V European Conference on Computational Fluid Dynamics
ECCOMAS CFD 2010
J. C. F. Pereira and A. Sequeira (Eds)
Lisbon, Portugal, 14–17 June 2010

NUMERICAL SIMULATION OF FLOW PAST A RECTANGULAR FLAT PLATE AT INCIDENCE

Dan Yang[*], Bjørnar Pettersen[†], Helge I. Andersson[††], and Vagesh D. Narasimhamurthy[§]

[*]Department of Marine Technology
Norwegian University of Science and Technology, NO-7491 Trondheim, Norway
e-mail: dan.yang@ntnu.no

[†] Department of Marine Technology
Norwegian University of Science and Technology, NO-7491 Trondheim, Norway
e-mail: bjornar.pettersen@ntnu.no

[††] Department of Energy and Process Engineering
Norwegian University of Science and Technology, NO-7491 Trondheim, Norway
e-mail: helge.i.andersson@ntnu.no

[§]Department of Energy and Process Engineering
Norwegian University of Science and Technology, NO-7491 Trondheim, Norway
e-mail: vagesh.d.narasimhamurthy@ntnu.no

Key words: Numerical Simulation, Flat Plate

Abstract. *Two-dimensional numerical simulation was employed to investigate the unsteady separated flow past a rectangular flat plate inclined with an angle of attack of 30 degrees to the mean flow. The rectangular flat plate characterized by a length-width ratio of 50 represents a marine bluff body, and is described by the immersed boundary method in our code. Two different flow cases were compared for the chosen angle of attack. In the first case, to achieve the attack angle, the flat plate was imposed by introducing an inclination relative to the Cartesian grid. In the second case the flat plate was fit to the grid and the incoming flow was inclined. These two cases both have their advantages and disadvantages according to the different grid implementation. The Reynolds number is 750 with the chord length of the plate as characteristic length scale. The results show that these two flow cases give almost the same vortices shedding alternately from leading edge and trailing edge with a shedding frequency corresponding to a Strouhal number of around 0.34. The steady mean flow was obtained by averaging in time.*

1 INTRODUCTION

Flow of a fluid past bluff bodies and particularly of two-dimensional bluff bodies have been extensively studied because of their relevance to drag on vehicles and flow over ship hulls and submarines. Such flows provide rich and interesting flow dynamics of considerable engineering relevance. Bluff bodies such as plates, discs, circular and rectangular cylinders and V-shaped prisms are used in combustors to enhance scalar mixing and provide a flame-stabilizing region [1]. Investigations on some classical configurations have been done both experimentally and numerically in order to try to understand the fundamental aspects of wakes and flow-induced vibration. The most significant parameter to characterize this kind of flow separation is the Reynolds number. The flow past a flat plate with different inclination angles (α) is characterized by fixed separation points at the edges of the plate. In some special parameter regions the flow status are very sensitive to the Reynolds number and angle of attack.

Incoming flow normal to the plate is the most studied (see Table 1). Unlike flow past a normal plate, the case with a tilting plate has different vortex shedding mechanism from the leading edge compare to the more complex shedding from the trailing edge. If we focus our attention on the tilting angle, it is surprising to see that almost all the inclined plate flow cases are either studied by experiments or by potential flow theory [2,3,4].

Case	Re	Angle α	Flow regime	Method
Fage and Johansen (1927) [5]	1.5×10^5	0-90°	Turbulence	Experiments
Lam (1996) [6]	3.0×10^4	30°	Turbulence	Experiments
Leder (1991) [7]	2.8×10^4	90°	Turbulence	Experiments
Breuer and Jovicic (2001) [8]	2.0×10^4	18°	Turbulence	3D-numerical
Breuer et al. (2003) [9]	2.0×10^4	18°	Turbulence	3D-numerical
Elder (1960) [10]	10^4-10^6	0°	Turbulence	Experiments
Crompton and Barrett (2000) [11]	10^4-5.4×10^5	0-90°	Turbulence	Experiments
Lam and Leung (2005) [13]	5300	20-30°	Turbulence	Experiments
Chen and Fang (1996) [12]	3.5×10^3-3.2×10^4	0-90°	Turbulence	Experiments
Najjar and Vanka (1995) [14]	1000	90°	Turbulence	3D-numerical
Narasimhamurthy and Andersson (2009) [15]	750	90°	Turbulence	3D-numerical
Knisely (1990) [16]	7.2×10^2-3.1×10^4	0-90°	Turbulence	Experiments
Najjar and Vanka (1995) [1]	100-1000	90°	Turbulence	2D-numerical
Najjar and Balachandar (1998) [17]	250	90°	Transition	3D-numerical
Taira et al. (2007) [18]	300	0-90°	Transition	3D-numerical & Experiments
Zhang et al. (2009) [19]	0-800	0-45°	Transition	2D-numerical
Jackson (1987) [20]	0-100	0-60°	Laminar	2D-numerical

Table 1: Various studies on flow past a flat plate with inclinations.

The earliest work concerned with vortex shedding from a sharp-edged plate was that of Fage & Johansen (1927) [5], dealing with the plate at 18 different angles of incidence. It is important to note that this geometry was not truly rectangular. Jackson (1987) [20] simulated the periodic behavior in two-dimensional laminar flow past various shapes of bodies including flat plates aligned over a range of angles to the direction of flow. Inclined plates at significant high Reynolds numbers are almost all investigated experimentally. Knisely (1990) [16] measured Strouhal numbers for a family of rectangular cylinders with side ratios ranging from 0.04 to 1.0 and with angles of attack

from 0° to 90°. Lam (1996) [6] investigated the flow past an inclined flat plate at α =15° using phased-averaged LDA measurements. The results showed that the train of trailing edge vortices has higher vortex strength than the train of leading edge vortices. The flat plates with sharp leading and trailing edges were also investigated [11, 12]. Breuer et al. [8, 9] simulated the flow over an inclined plate at α =18° and the computational results showed clearly that the wake is strongly dominated by the trailing edge vortices. It was also reported that there is no regular shedding motion of rotating vortices directly at the leading edge. Instead, behind the leading edge, a Kelvin-Helmholtz instability is detected in the free shear layer. These shear layer vortices develop into a large recirculation region attached to the leeward side of the plate. Zhang et al. (2009) [19] studied the transition route from steady to chaotic state for flow past an inclined flat plate and the results reveal a transition process via the sequential occurrence of the period-doubling bifurcations and the various incommensurate bifurcations.

The present study has the same geometry of the plate as used by Narasimhamurthy and Andersson (2009) [15] except the attack angle in order to investigate the different vortex shedding from the leading and trailing edges respectively.

2 NUMERICAL PROCEDURE

2.1 Governing equations and numerical method

The dynamics of an incompressible Newtonian fluid can be completely described by the Navier-Stokes equations. The non-dimensionalized mass and momentum equations written in vector form are

$$\nabla \cdot \mathbf{u} = 0 \tag{1}$$

$$\frac{\partial \mathbf{u}}{\partial t} + (\mathbf{u} \cdot \nabla)\mathbf{u} = -\nabla p + \frac{1}{Re}\nabla^2 \mathbf{u} \tag{2}$$

The equations are non-dimensionalized by the plate length d and the freestream velocity U_0. The Reynolds number is defined as $Re = U_0 d/\nu = 750$, where ν is the kinematic viscosity. In the above equations $\mathbf{u} = \{u,\ v\}$ is the instantaneous velocity field, p is the non-dimensional pressure and t represents the non-dimensional time scaled by (d/U_0).

The governing equations were solved in two-dimensional space and time using a parallel finite-volume code called MGLET (Manhart, 2001, [21]; Manhart et al, 2004, [22]) with the staggered Cartesian grid arrangements. The spatial derivatives were discretized by means of a 2nd-order central-difference scheme. The time marching was carried out using a 3rd-order explicit Runge-Kutta scheme for the momentum equations in combination with an iterative SIP (Strong Implicit Procedure) solver for the Poisson equation.

The bluff body (flat plate) was implemented on the Cartesian mesh by Immersed Boundary Method (IBM) [23]. In this method the non-slip condition was transformed from the solid body's surfaces into internal boundary conditions at the nodes of the staggered grid by direct forcing. The rectangular inclined flat plate was represented by a mesh consisting of triangles. The internal boundary condition value had to be determined by interpolation.

2.2 Flow configuration and computational details

With the Cartesian mesh and IBM a solid body surface with curvature is not smoothly represented. A flat plate's surface is also rough when the plate is tilted with respect to the mesh. In the present simulation a computational domain with the plate immersed tilted to the structured grid by 30 degree was used (Case 1). For this case it is convenient to get the blockage ratio and the inflow velocity parallel to the streamwise mesh. To achieve the smooth result on the plate surfaces a case with the same plate immersed and overlapped on the grid was also simulated (Case 2). For the second case the angle of attack was achieved by totally different boundary implementations (see Table 2). Considering all these different characteristics, the two cases were simulated. The size of the computational domains in the streamwise (x) and cross-stream (y) direction and the position of plate were normalized by d, as shown in figure 1. d_1 is the projected length of the plate perpendicular to the main flow direction. All velocities were scaled by the uniform inflow velocity U_0. The thickness of the plate was very small and equal to $0.02d$ [15].

	LEFT	RIGHT	TOP	BOTTOM
Case1	$u = U_0$ $v = 0$ $\frac{\partial p}{\partial x} = 0$	$\frac{\partial u}{\partial x} = 0$ $\frac{\partial v}{\partial x} = 0$ $p = 0$	$\frac{\partial u}{\partial y} = 0$ $v = 0$ $\frac{\partial p}{\partial y} = 0$	$\frac{\partial u}{\partial y} = 0$ $v = 0$ $\frac{\partial p}{\partial y} = 0$
Case2	$u = \cos\alpha \cdot U_0$ $v = \sin\alpha \cdot U_0$ $\frac{\partial p}{\partial x} = 0$	$\frac{\partial u}{\partial x} = 0$ $\frac{\partial v}{\partial x} = 0$ $p = 0$	$\frac{\partial u}{\partial y} = 0$ $\frac{\partial v}{\partial y} = 0$ $p = 0$	$u = \cos\alpha \cdot U_0$ $v = \sin\alpha \cdot U_0$ $\frac{\partial p}{\partial y} = 0$

Table 2: Boundary conditions for the two different cases.

Table 3 shows the various grid properties and domain sizes considered in this study. The time step size was set to $0.001d/U_0$ in both calculations, which kept the maximum convective CFL number below 0.3 on the finest grid.

Case	$N_x \times N_y$	$[x_u,\ x_d]$[1]	$[y_b,\ y_t]$[2]	Δx_{min}	$\Delta x^u_{max}\ (\Delta x^d_{max})$[3]	Δy_{min}	$\Delta y^b_{max}\ (\Delta y^t_{max})$[4]
Case 1	704×474	[5, 20]	[8, 8]	0.01	0.22(0.04)	0.01	0.06(0.06)
Case 2	768×855	[5, 20]	[5, 15]	0.01	0.22(0.03)	0.01	0.12(0.02)

[1] x_u and x_d are the upstream and downstream distance measured from the plate center respectively.

[2] y_b and y_t are the bottom and top widths measured from the plate center respectively.

[3] Δx^u_{max} and Δx^d_{max} are the maximum grid sizes upstream and downstream of the plate respectively.

[4] Δy^b_{max} and Δy^t_{max} are the maximum grid sizes at the bottom and top of the plate respectively.

Table 3: Summary of grid resolution and extent of computational domain.

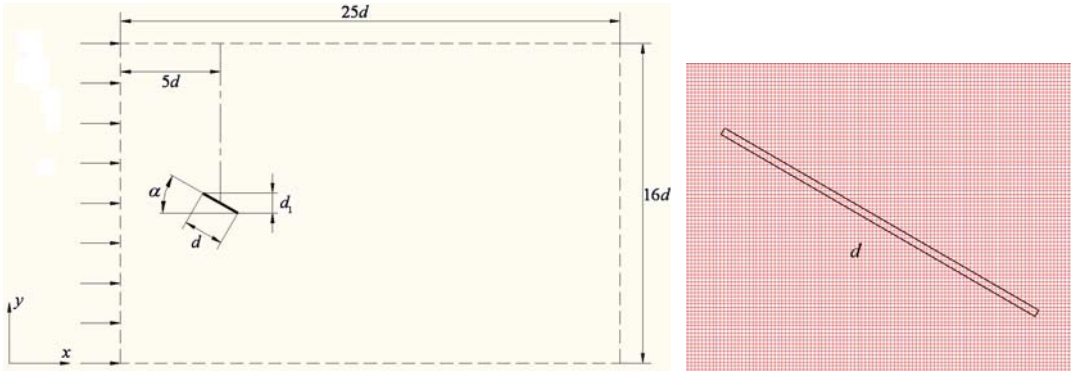

(a) Case 1.

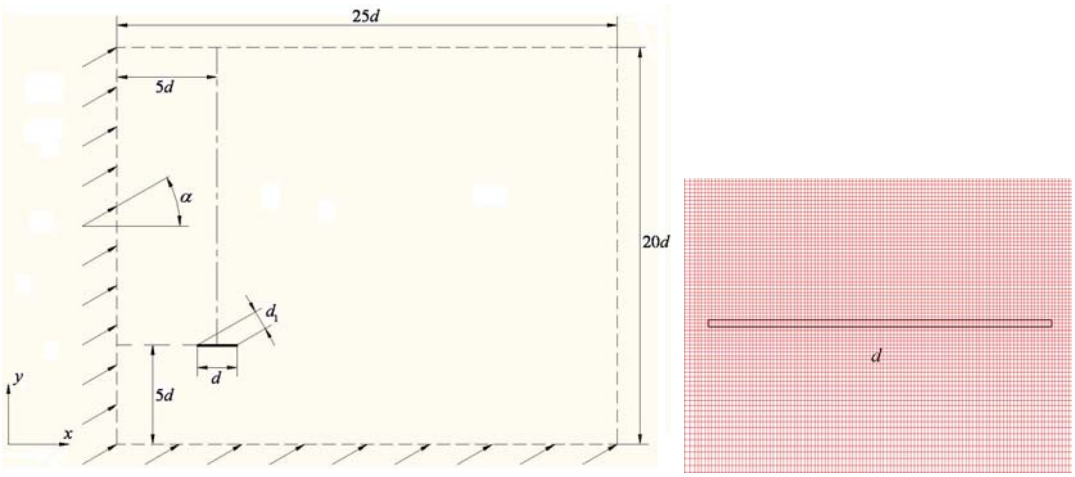

(b) Case 2.

Figure 1: Computational domain and mesh.

3 RESULTS

Comparisons were made between Case 1 and Case 2.

3.1 Time-averaged flow variables

Time-averaged statistical quantities were evaluated by sampling for $200\,d/U_0$ time units. Each sample is taken every tenth time step for averaging. Figure 2 presents the time-averaged streamlines behind the inclined plate. The flow separates at the leading edge and forms a large clockwise rotating recirculation region on the leeward side of the plate (B). Whereas the trailing edge vortex resides upon the end of the plate (D). These two types of vortices form a stagnation point closer to the trailing edge (C). There is also a small anti-clockwise rotating recirculation region between the clockwise recirculation and the plate (A). The position of this small recirculation is attributed to the chosen attack angle.

The different locations of and pressure at the characteristic points (A, B, C and D) shown in Fig. 2 in the two simulations are compared in Table 4. The positions were measured from the leading edge and scaled with the plate length d. Apparently these two simulations are quite close. This circumstance is also clearly visible in figure 3, which shows the time-averaged pressure contours and streamlines around the plate.

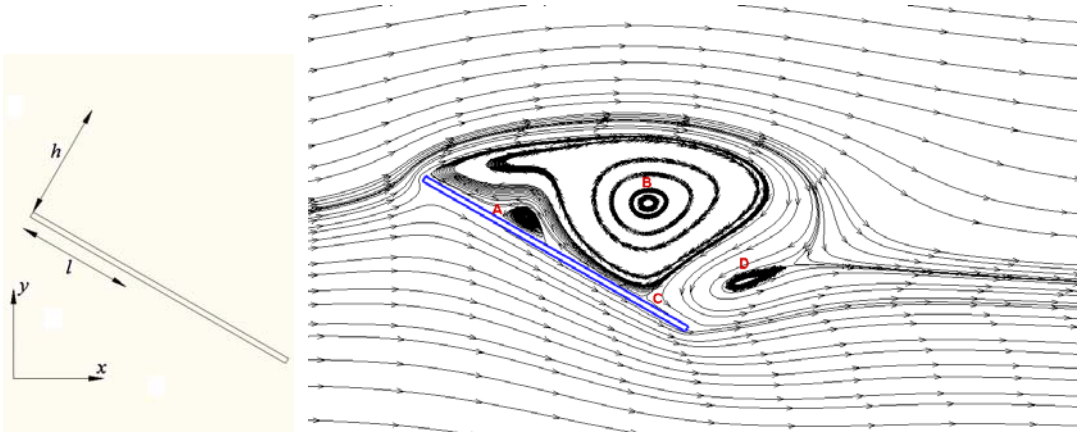

Figure 2: Mean flow field recirculation shape.

		A	B	C	D
Case1	l/d	0.3552	0.6805	0.8249	1.0856
	h/d	0.0501	0.2873	0.0	0.2217
	$p/\rho U_0^2$	-0.5465	-0.7027	-0.3283	-1.0736
Case2	l/d	0.3340	0.6731	0.8263	1.0959
	h/d	0.0564	0.2887	0.0	0.2249
	$p/\rho U_0^2$	-0.5949	-0.7864	-0.5706	-1.1961

Table 4: Different positions and pressure at the points (A, B, C and D) in Fig.2.

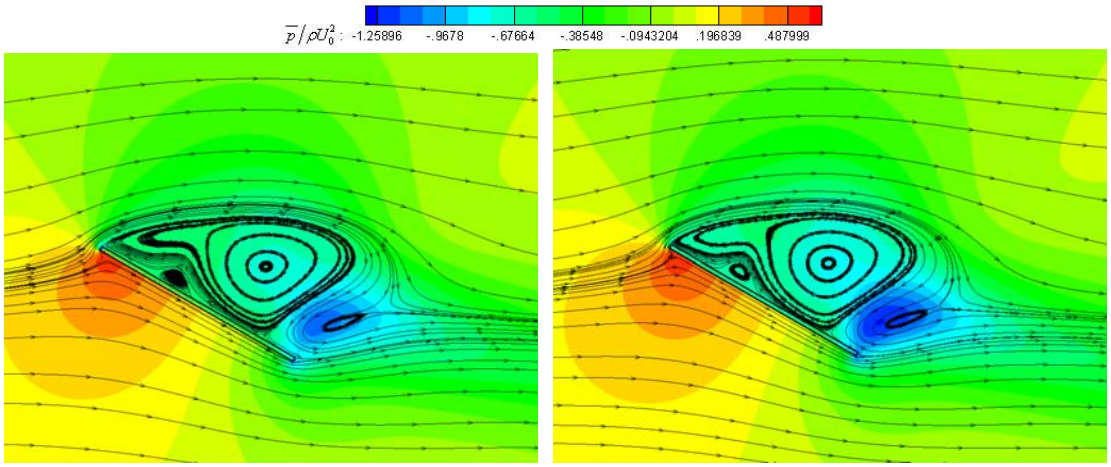

(a) Case 1. (b) Case 2.

Figure 3: Pressure contours and streamlines.

The mean pressure coefficient is defined as

$$\overline{C_p} = \frac{\overline{p} - p_\infty}{1/2\,\rho U_0^2} \tag{3}$$

Where the reference pressure p_∞ is taken from the pressure at the inflow and the bar means averaging in time. The distribution of $\overline{C_p}$ on the surface of the plate from the present two simulations is compared with the earliest experimental data in figure 4. The

pressure on the front surface of the plate compares well with the previous data. However, on the rear surface the pressure is relatively lower compared to the experiment and the difference is larger near the trailing edge both on the front and rear surface. This could be a 2D-simulation and Reynolds number effect. The vortex on the rear surface of the plate leads to a pronounced minimum close to the trailing side, which also could be a 2D-simulation effect as said before. The pressure in the large recirculation region is nearly constant.

Comparing the present two simulations, the pressure is a little lower in the second case especially on the rear surface. This will cause higher drag and lift forces on the plate. Table 5 provides a comparison of integral quantities and frequency for the flat plate in the present simulations and 2D numerical results of Breuer and Jovicic (2001) [8]. The drag and lift forces are higher in the second case as expected because of the lower pressure which contribute to the main part in these two forces. Because the angle of attack and Reynolds number are different, the drag force is higher and the lift force is lower than Ref. [8].

Figure 5 shows the distribution of the friction coefficient $\left(\overline{C_f}\right)$ along the plate for the time-averaged flow, $\left(\overline{C_f}\right)$ is defined as

$$\overline{C_f} = \frac{\overline{\tau_w}}{1/2\,\rho U_0^2} \tag{4}$$

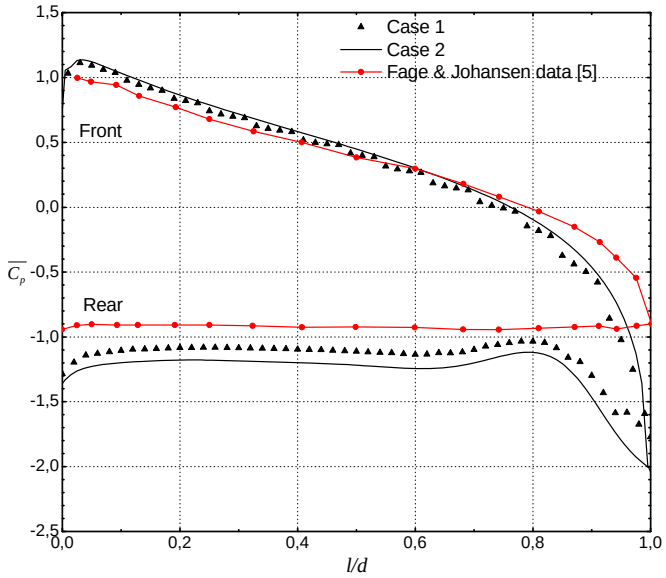

Figure 4: Pressure coefficient distribution on flat plate.

	Re	α	$\left(\overline{C_L}\right)^1$	$\left(\overline{C_D}\right)^2$	$(St)^3$	$(St')^4$
Case1	750	30°	1.2714	0.6874	0.3412	0.1706
Case2	750	30°	1.3220	0.7191	0.3455	0.1728
Breuer and Jovicic (2001) [8]	2.0×10^4	18°	1.69	0.57	0.45	0.139

[1] $\overline{C_L} = 2F_L/\left(\rho U_0^2 d\right)$ is the time-averaged lift coefficient of the plate, where F_L is the lift force.

[2] $\overline{C_D} = 2F_D/\left(\rho U_0^2 d\right)$ is the time-averaged drag coefficient of the plate, where F_D is the drag force.

[3] $St = fd/U_0$ and [4] $St' = fd_1/U_0$ are Strouhal number base on different length scales.

Table 5: Comparison of integral quantities and frequency for the flat plate.

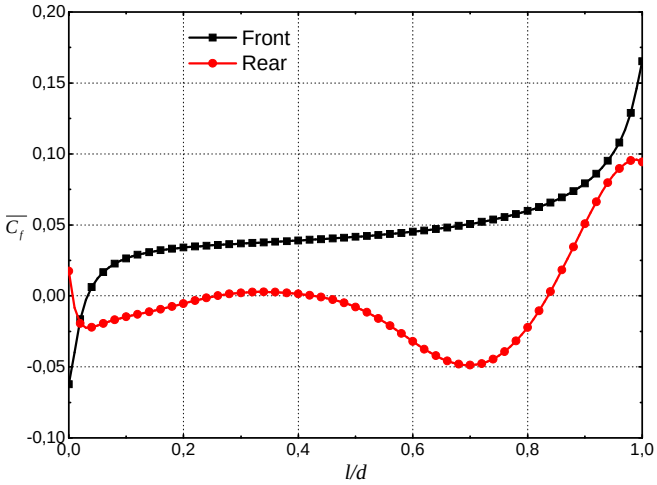

Figure 5: Friction coefficient distribution on the flat plate (Case 2).

The profiles of the tangential velocity component on the front and rear sides of the inclined plate are depicted in figure 6 for the time-averaged flow field. On the rear side of the plate the profile exhibits an upstream fluid flow along the plate except close to the trailing edge. This is consistent with the distribution of the friction coefficient $\overline{C_f}$ shown in figure 5. Combining both figures it becomes clear that the fluid at the rear side of the plate move with a variable velocity towards the leading edge. As expected the flow is accelerated along the front side of the plate, and there is a stagnation point on the front side close to the leading edge.

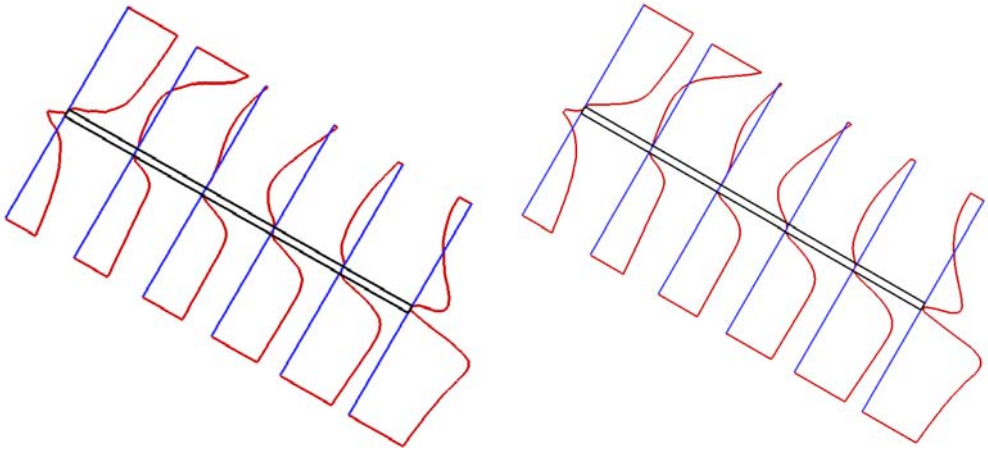

(a) Case 1. (b) Case 2.

Figure 6: Tangential velocity distribution on flat plate.

3.2 Wake pattern and frequency analysis

The vorticity fields both time-averaged and instantaneous are shown in figure 7. The red color denotes the clockwise rotation while the blue color means counter-clockwise rotation. As can be seen in figure 7(b) and (c), the vortices generated from the leading edge almost align in one line and decrease in strength (see figure 7(a)). The clockwise vortex separated from the leading edge is split into two parts where the second is attracted to the counter-clockwise vortex generated from the trailing edge. The vortex pair moves downstream and has a counter-clockwise rotation. When they reach the lowest position in the vertical direction, at $x/d = 16 \sim 18$, the clockwise vortex is

approximately right under the counter-clockwise vortex. The vortex pair then moves upwards while they still rotate anti-clockwise. This vertical oscillating motion varies with the inclined angle of the plate. The lowest position may be different as the angle of attack changes (not shown here).

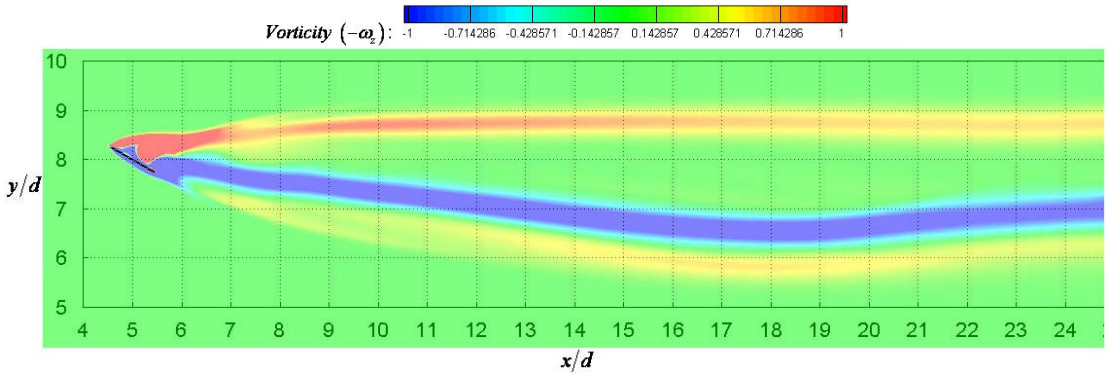

(a) Mean vorticity.

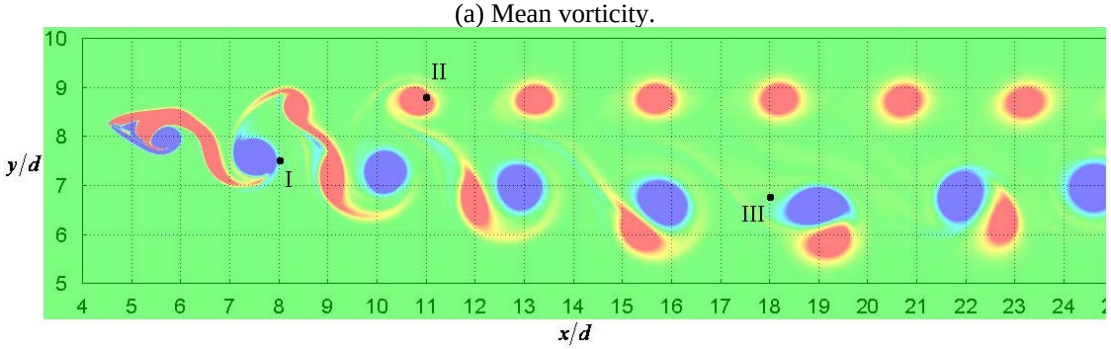

(b) Instantaneous vorticity from Case 1.

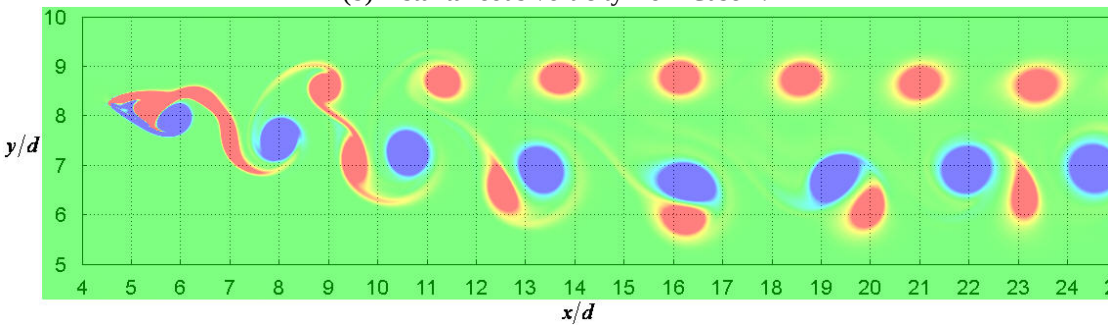

(c) Instantaneous vorticity from Case 2.

Figure 7: Mean and instantaneous vorticity in the wake.

This phenomenon can also be seen from the mean vorticity field in figure 7(a). The time-averaged vorticity figure gives more clearly the vortex strength and position in the wake.

The mean velocity profiles at different fixed x/d positions are presented in figure 8 in order to compare the details of the two simulations. The streamwise velocity at the location $x/d = 6$ is very low since this position is very close to the recirculation zone. Because of the oscillating position of the vortex pairs, the low velocity region enlarges along the wake. At $x/d = 18$ this region is at its largest in the wake (can also be seen from figure 7(a)).The maximum streamwise velocity along the vortex pair side becomes higher before the vortex pair moves up again. The discrepancy of the mean streamwise velocity between the two simulations seems to be larger far away from the plate. This

tendency can also be seen from the mean streamwise velocity profile at the centerline of the plate as a function of x/d in figure 9(a). The mean cross-stream velocity shown in figure 9(b) does not show the same tendency. The boundary conditions setup in the two simulations could be the explanation for the different tendency.

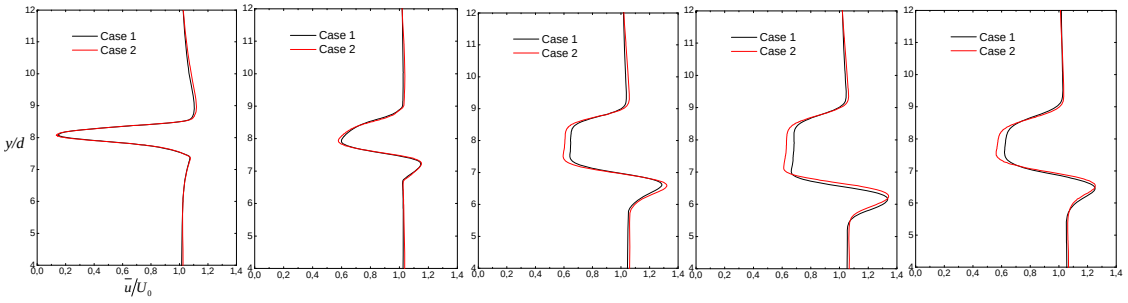

(a) $x/d = 6$. (b) $x/d = 8$. (c) $x/d = 13$. (d) $x/d = 18$. (e) $x/d = 23$.

Figure 8: Mean velocity profile at fixed x/d positions.

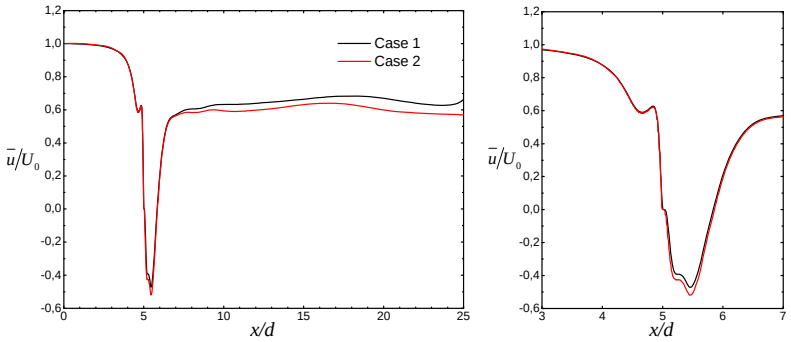

(a) Mean streamwise velocity ($\bar{u}/U_0$) and details over the plate to the right.

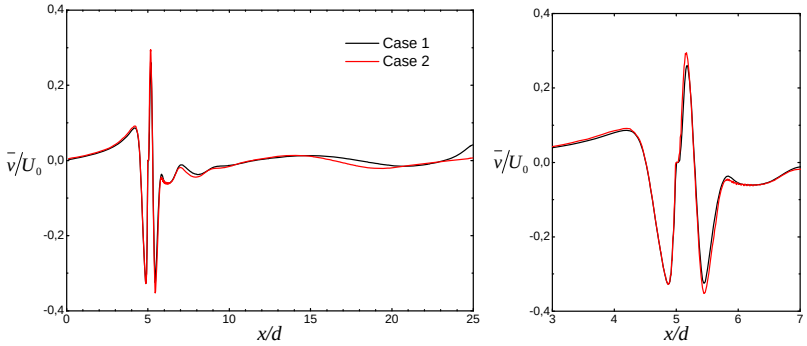

(b) Mean cross-stream velocity ($\bar{v}/U_0$) and details over the plate to the right.

Figure 9: Mean velocity at the centerline of the plate along the streamwise direction.

The time evolution of the instantaneous velocity components $\{u, v\}$ and the instantaneous pressure p (not shown in the paper) were sampled along the two trailing vortices in the wake. Here the time trace of the streamwise velocity sampled at three different points (see point I, II and III in figure 7(b)) are shown in figure 10. The total sampling time was equal to $200\,d/U_0$, which covers about 60 vortex shedding cycles. To enable quantitative comparisons the power spectral density (PSD) was obtained from the streamwise velocity time trace and the phase-space of velocity components was plotted. The plots in figure 10(a) are for the point II located in the upper leading edge

vortices area. The PSD figure and phase-space plot give clearly one frequency at 0.34 which is consistent with aforementioned figures and the Strouhal number (St) in table 5. The plots in figure 10(b) and (c) are for point I and III located in the lower trailing edge vortices area. There should be two main frequencies in this area, but because the vortex pairs rotate, it is difficult to capture two frequencies all along the vortex trace. Figure 10(b) gives one of these points (point I), whereas the point III in 10(c) has one main frequency even though it is located in the same vortex street.

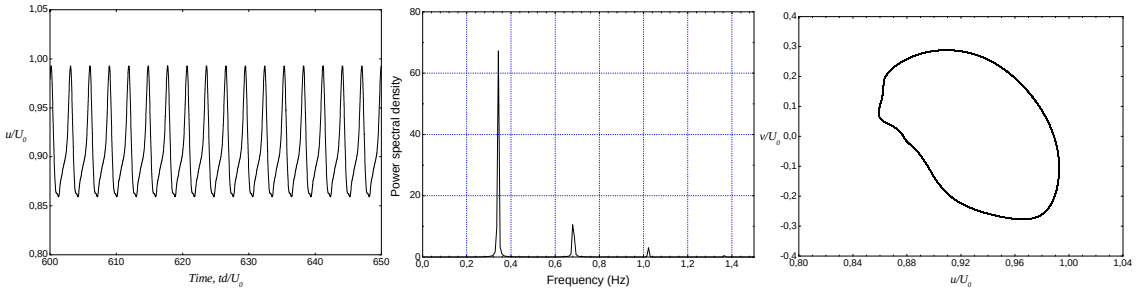

(a) Point II: $x/d = 11$, $y/d = 8.8$.

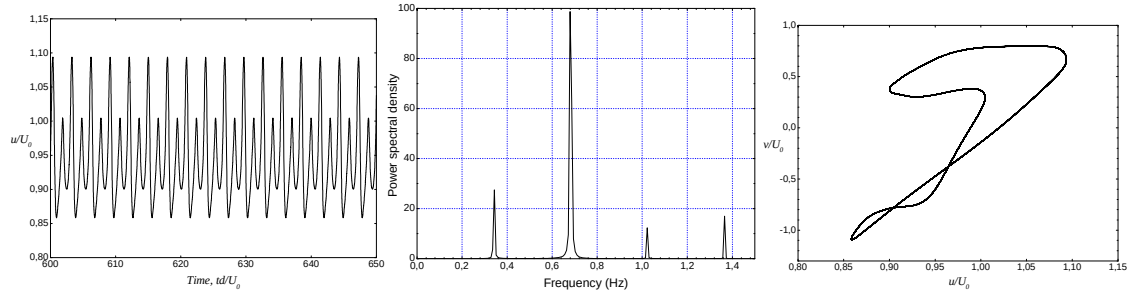

(b) Point I: $x/d = 8$, $y/d = 7.5$.

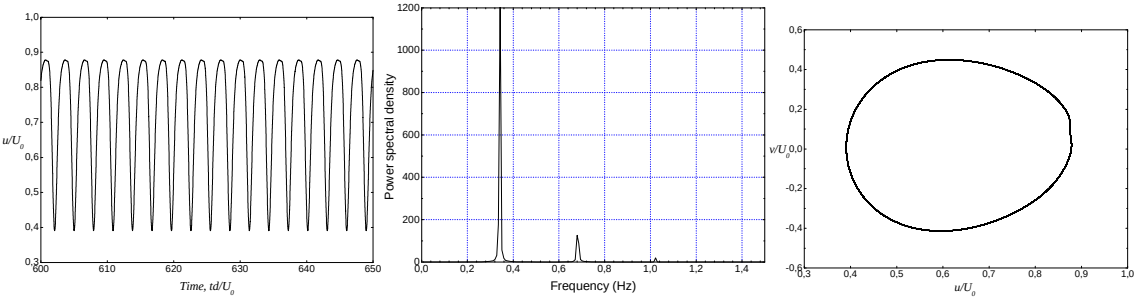

(c) Point III: $x/d = 18$, $y/d = 6.8$.

Figure 10: Left: streamwise velocity time history (only a portion of the total time-traces are shown here); Center: power spectrum density of the streamwise velocity, and; Right: phase-space plot of the velocity components $(u,\ v)$ at different points in the wake.

4 CONCLUSIONS

The two-dimensional numerical simulations with different numerical implementations were used to capture the shedding characteristics of the wake behind a flat plate inclined at an angle of 30 degrees. The details in the results were compared and it turned out that the flows near the plate are quite consistent. The measured base pressure from experiment was relatively higher compared to the present calculations

especially at the rear side close to the trailing edge of the plate. The reason for this discrepancy may be due to the 2D-simulation effect and different Reynolds number considered in the present study and in Fage & Johansen (1927) [5]. A detailed analysis of the wake was presented. It was noticed that a clockwise vortex separated from the leading edge vortex was attracted to the main counter-clockwise vortex generated from the trailing edge and formed a vortex pair moving downstream while rotating. Almost all the results for Case 2, in which the plate was implemented aligned with the Cartesian grid lines, compared favorably with the results of the more straightforward implementation used in Case 1. The reason for the modest discrepancy in the far wake velocities could be due to the different boundary conditions adopted in the two simulations. The time trace of velocity component at different positions in the wake captured two types of shedding frequencies as expected.

REFERENCES

[1] F.M. Najjar and S.P. Vanka, Simulations of the unsteady separated flow past a normal flat plate. *Int. J. Num. Meth. Fluids* **21** , pp. 525-547 (1995)

[2] M. Kiya and M. Arie, An inviscid numerical simulation of vortex shedding from an inclined flat plate in shear flow. *J. Fluid Mech.* **82** , pp. 241-253 (1977)

[3] M. Kiya and M. Arie, A contribution to an inviscid vortex-shedding model for an inclined flat plate in uniform flow. *J. Fluid Mech.* **82** , pp. 223-240 (1977)

[4] W.W.H. Yeung and G.V. Parkinson, On the steady separated flow around an inclined flat plate. *J. Fluid Mech.* **333** , pp. 403-413 (1997)

[5] A. Fage and F.C. Johansen, On the flow of air behind an inclined flat plate of infinite span. *Brit. Aero. Res. Coun. Rep. Memo.* **1104** , pp. 81-106 (1927)

[6] K.M. Lam, Phase-locked eduction of vortex shedding in flow past an inclined flat plate. *Phys. Fluids* **8** , pp. 1159-1168 (1996)

[7] A. Leder, Dynamics of fluid mixing in separated flows. *Phys. Fluids A.* **3** , pp. 1741-1748 (1991)

[8] M. Breuer and N. Jovicic, Separated flow around a flat plate at high incidence: an LES investigation. *J. Turbulence* **2** , pp. 1-15 (2001)

[9] M. Breuer, N. Jovicic and K. Mazaev, Comparison of DES, RANS and LES for the separated flow around a flat plate at high incidence. *Int. J. Num. Meth. Fluids* **41** , pp. 357-388 (2003)

[10] J.M. Elder, The flow past a flat plate of finite width. *J. Fluid Mech.* **9** , pp. 133-153 (1960)

[11] M.J. Crompton and R.V. Barrett, Investigation of the separation bubble formed behind the sharp leading edge of a flat plate at incidence. *Proc. Inst. Mech. Engrs.* **214** , Part G, pp. 157-176 (2000)

[12] J.M. Chen and Y.-C. Fang, Strouhal numbers of inclined flat plates. *J. Wind Eng. Ind. Aerodyn.* **61** , pp. 99-112 (1996)

[13] K.M. Lam and M.Y.H. Leung, Asymmetric vortex shedding flow past an inclined flat plate at high incidence. *Euro. J. Mech. B/Fluids* **24** , pp. 33-48 (2005)

[14] F.M. Najjar and S.P. Vanka, Effects of intrinsic three-dimensionality on the drag characteristics of a normal flat plate. *Phys. Fluids* **7** , pp. 2516-2518 (1995)

[15] V.D. Narasimhamurthy and H.I. Andersson, Numerical simulation of the turbulent wake behind a normal flat plate. *Int. J. Heat Fluid Flow* **30** , pp. 1037-1043 (2009)

[16] C.W. Knisely, Strouhal numbers of rectangular cylinders at incidence: a review and new data. *J. Fluid Structures* **4** , pp. 371-393 (1990)

[17] F.M. Najjar and S. Balachandar, Low-frequency unsteadiness in the wake of a normal flat plate. *J. Fluid Mech.* **370** , pp. 101-147 (1998)

[18] K. Taira, W.B. Dickson, T. Colonius and M.H. Dickinson, Unsteadiness in flow over a flat plate at angle-of-attack at low Reynolds numbers. In proceedings of the *45th AIAA Aerospace Sciences Meeting and Exhibit.* AIAA Paper 2007-710 (2007)

[19] J. Zhang, N.-S. Liu and X.-Y. Lu, Route to a chaotic state in fluid flow past an inclined flat plate. *Phys. Review.* **E. 79** , pp. 045306: 1-4 (2009)

[20] C.P. Jackson, A finite-element study of the onset of vortex shedding in flow past variously shaped bodies. *J. Fluid Mech.* **182** , pp. 23-45 (1987)

[21] M. Manhart, F. Tremblay and R. Friedrich, MGLET: a parallel code for efficient DNS and LES of complex geometries. In proceedings of the *12th International Conference on Parallel Computational Fluid Dynamics*, C.B. Jenssen et al. Elsevier Science B.V.: Amsterdam, pp. 449-456 (2001)

[22] M. Manhart, A zonal grid algorithm for DNS of turbulent boundary layers. *Comput. Fluids* **33** , pp. 435-461 (2004)

[23] N. Peller, A.L. Duc, F. Tremblay and M. Manhart, High-order stable interpolations for immersed boundary methods. *Int. J. Num. Meth. Fluids* **52** , pp. 1175-1193 (2006)